Corrosion Science 167 (2020) 108492

Contents lists available at ScienceDirect

Corrosion Science

journal homepage: www.elsevier.com/locate/corsci

High-performance Cr_2AlC MAX phase coatings: Oxidation mechanisms in the 900–1100°C temperature range

Zhenyu Wang[a,c], Guanshui Ma[a], Linlin Liu[a], Li Wang[a,c], Peiling Ke[a,b,*], Qunji Xue[a], Aiying Wang[a,b,c,*]

[a] Key Laboratory of Marine Materials and Related Technologies, Zhejiang Key Laboratory of Marine Materials and Protective Technologies, Ningbo Institute of Materials Technology and Engineering, Chinese Academy of Sciences, Ningbo 315201, China
[b] Center of Materials Science and Optoelectronics Engineering, University of Chinese Academy of Sciences, Beijing, 10049, China
[c] Ningbo Institute of Industrial Technology, Chinese Academy of Sciences, Ningbo 315201, China

ARTICLE INFO

Keywords:
A. Ceramic
A. Metal coatings
B. XRD
B. TEM
C. Oxidation

ABSTRACT

Dense and predominantly single-phase Cr_2AlC MAX phase coatings without columnar structure were fabricated using an easy combined arc/sputtering deposition method followed by annealing. Isothermal oxidation of coatings was conducted under flowing air for 40 h at 900 − 1100 °C. Although the results revealed that the oxide scale showed strong dependence upon oxidation temperature, the coated samples remained intact even after oxidation at 1100 °C. Such excellent resistance to oxidation resulted in the parabolic kinetics exhibiting two stages. This was attributed to the formation of a dense and continuous Al_2O_3 interface layer and a $(Cr, Al)_2O_3$ outermost layer.

1. Introduction

Cr_2AlC belongs to a novel family of ternary layered compounds with the general formula $M_{n+1}AX_n$ (n = 1–3), called MAX phases (space group $P6_3/mmc$), where M is an early transition metal, A is predominantly a IIIA or IVA element, and X is C or N [1]. As one member of the M_2AlC family, Cr_2AlC possesses the highest bulk modulus compared with other materials (M = Ti, V, Nb, Ta), due to the Cr-C bond energy being the largest compared to other transition metal materials [2]. Moreover, it benefits from the combined properties of ceramics and metals, possessing high thermal-shock resistance, high electrical conductivity, and strong resistance to damage. It is easily machined as a metal, lightweight (5.24 g/cm^3), refractory, and has high elastic stiffness as a ceramic [3,4]. Therefore, as a promising candidate for high-temperature applications, Cr_2AlC has received considerable attention since it was first identified in the 1980s [5–7]. Very recently, Huang and colleagues demonstrated that Cr_2AlC exhibited high tolerance to 500 keV He^{2+} and 7 MeV Xe^{26+} ion irradiation damage induced by a 320 kV high-voltage platform [8]. Because of these superior thermal and mechanical properties as well as ion radiation tolerance, Cr_2AlC has the potential to be a structural material in nuclear reactors or as a protective coating material in accident tolerant fuel (ATF) systems [9] and other harsh environments [10].

In contrast to the expected high performance as bulk materials, however, Cr_2AlC coatings always present with relatively poor oxidation resistance, because of the columnar structure and growth defects (e.g. pin-holes, pores and other open voids) formed by traditional physical vapor deposition (PVD) techniques, including magnetron sputtering and cathodic arc. Wang et al. [11] deposited Cr_2AlC coatings on a β-γ TiAl alloy substrate and studied the oxidation resistance at temperatures of 700 and 800 °C. The premature failure of coatings only after about 100 h oxidation at 800 °C was attributed to the open voids along columnar boundaries and the limited Al reservoir in thinner coatings. Li et al. [12] investigated the oxidation resistance behavior of Cr_2AlC coatings on M38G substrates at higher temperatures of 900 − 1100 °C for 20 h. A large number of columnar grain boundaries also emerged in their coatings, through which nitrogen and oxygen inwardly diffused more rapidly from the surface, causing the degradation of coatings after short-term oxidation at 1000 °C. Until now, the oxidation mechanism of Cr_2AlC coatings at relatively long-term and high temperatures exceeding 1000 °C has not been fully examined.

Reports on the dependence of oxidation resistance of bulk Cr_2AlC MAX phase ceramics on the protective layer of surface oxide have been contradictory. Lin et al. [13] studied the oxidation properties of Cr_2AlC bulk materials at 800 − 1300 °C for 20 h in air. They demonstrated that the oxidation kinetics of Cr_2AlC followed a parabolic relationship, and

* Corresponding authors at: Key Laboratory of Marine Materials and Related Technologies, Zhejiang Key Laboratory of Marine Materials and Protective Technologies, Ningbo Institute of Materials Technology and Engineering, Chinese Academy of Sciences, Ningbo 315201, China.
E-mail addresses: kepl@nimte.ac.cn (P. Ke), aywang@nimte.ac.cn (A. Wang).

https://doi.org/10.1016/j.corsci.2020.108492
Received 5 September 2019; Received in revised form 13 December 2019; Accepted 23 January 2020
Available online 24 January 2020
0010-938X/

the scale that was formed composed of a homogenous and continuous outer Al_2O_3-rich layer. However, Li et al. [14] found only a dense Al_2O_3 scale without the appearance of Cr_2O_3 on Cr_2AlC bulk materials after 100 h oxidation at 1100 − 1200 °C in air. Cui et al. [15] claimed that the microstructure of the MAX phase had a significant influence on the formation of the surface oxide. As a consequence, the characterization and corrosion behavior of oxide scale formed on Cr_2AlC coating surface including chemical composition, microstructure, and thickness should be clarified, especially in light of differences between the bulk MAX phase ceramics and relatively thin coatings.

In this study, dense and predominantly single-phase Cr_2AlC MAX phase coatings were successfully fabricated by a homemade combination of arc/sputtering deposition. To explore their application in high temperature systems in particular, we focused on the oxidation resistance of coatings at 900 − 1100 °C for 40 h, which was the longest oxidation time at temperatures exceeding 1000 °C for MAX phase coatings as reported in the literature. The oxidation mechanism of Cr_2AlC coatings will also be discussed in terms of the characterization of oxide scale and the microstructural evolution of the coatings during oxidation.

2. Experimental procedure

2.1. Preparation of Cr_2AlC coatings

The Cr_2AlC MAX phase coatings were fabricated on Hastelloy substrates (15 mm × 10 mm × 5 mm) using a home-made combined arc/sputter technology, followed by vacuum annealing. The nominal composition of Hastelloy (%wt) was: Cr, 23; Mo, 16; Mn, 0.5; Si, 0.08; C, 0.01, and the balance Ni. Substrates were cleaned ultrasonically in acetone and then alcohol for 15 min before being loaded into the vacuum chamber. The rectangular aluminum target (purity: 99.9 %; 400 mm × 100 mm × 7 mm) and the circular chromium target (purity: 99.9 %; diameter 128 mm × 15 mm) were applied as sputtering source and cathode arc source, respectively. The schematic diagram of this deposition system is depicted in Fig. 1. All eight substrates were suspended 3 cm apart on a pre-fixed rack by iron wire. Prior to deposition, the deposition chamber was evacuated to a base pressure of 1.5×10^{-3} Pa to eliminate air. The chamber was then heated to 200 °C. To improve the adhesion strength, all substrates were pre-etched by Ar^+ bombardment for 60 min, and then a Cr interlayer (thickness of ~1000 nm) was deposited by pure arc technology. During Cr-Al-C coatings deposition, gas mixtures of Ar and CH_4 (flow rate ratio: Ar/CH_4 = 3/40), at a total pressure of 1.9 Pa, were used as reactive gas. To ensure all substrate faces were coated uniformly, the substrates were rotated on their axis in the front of Al targets, with a substrate distance of 5 cm. During deposition, the power of Cr and Al targets was kept at 17 W and 2.85 kW, respectively. Substrate negative bias voltage of −200 V was applied to the substrate during both etching and deposition processes, and the deposition temperature was kept at 200 °C. After deposition, to transform the Cr-Al-C coatings to Cr_2AlC MAX phase coatings, a vacuum annealing treatment was applied to the Cr-Al-C coatings at 700 °C for 5 h under a vacuum of 1.0×10^{-3} Pa.

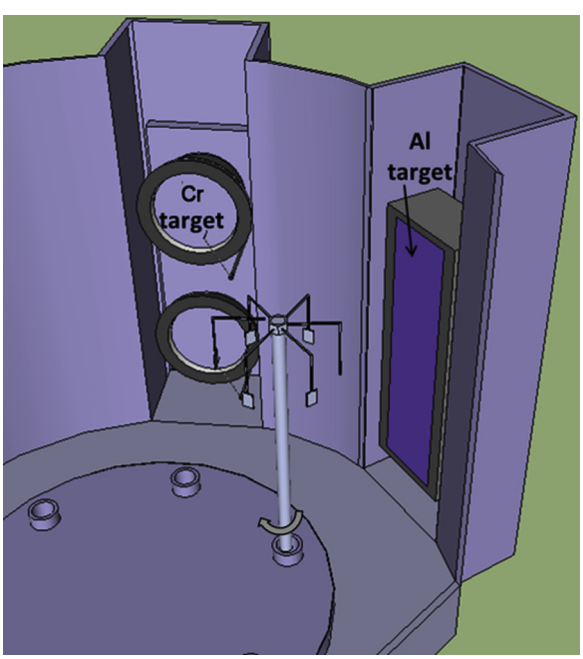

Fig. 1. Schematic diagrams of the coating deposition system.

2.2. Oxidation and characterization methods

The isothermal oxidation experiment was conducted using a thermos balance (Setsys Evolution TGA/STA-EGA) with flowing synthetic air (20 % O_2, 80 % N_2) with a flow rate of 20 ml/min. The samples were suspended by Pt wire and heated to the target temperature (900, 1000 and 1100 °C) at a rate of 20 °C/min. During the experiments, the mass gains of the samples were recorded continuously as a function of annealing time. Thermal shock resistance tests at 1100 °C were applied to determine the adhesion of the oxidized coatings to the substrates. The oxidized coatings were heated to 1100 °C in a tube furnace for 10 min, subsequently rapidly cooled in deionized cold water for 5 min, then returned to the furnace for the next cycle.

Surface and cross-sectional morphologies of the as-prepared Cr_2AlC coatings and the oxidized coatings were characterized by scanning electron microscopy (SEM). Analytical SEM was conducted at 15 kV using a field emission FEI Quanta FEG 250 equipped with a backscatter electron (BSE) detector and an Oxford energy-dispersive spectrometer (EDS). Phase identifications of the as-prepared and the oxidized Cr_2AlC coatings were made by X-ray diffraction (XRD; D8-Advance Brucker) using Cu Kα radiation (λ = 1.5406 Å) at a scanning rate of 0.5 °/min and 2θ angle from 10° to 90°. Transmission electron microscopy (TEM), high resolution TEM (HRTEM), selected-area electron diffraction (SAED), and scanning TEM (STEM) characterizations were accomplished with a Talos F200X operating at 200 kV equipped with an EDS detector and a high-angle annular dark field (HAADF) detector. Specimens for TEM were prepared by focused ion beam (FIB) lift-out methods using a Zeiss Auriga dual-beam FIB/SEM. Details of TEM sample preparation using FIB were given in [16].

3. Results

3.1. Microstructure of the prepared Cr_2AlC coatings

X-ray diffraction analyses of the as-prepared Cr_2AlC coatings identified the three crystalline phases as being Cr_2AlC, Al_4C_3 and Cr_3C_2, indexed by PDF card No. 29-0017, 35-0799 and 35-0804, respectively (Fig. 2). To quantitatively identify the content of these determined phases, the technique of Rietveld refinement was applied to the diffraction patterns [17]. Several refinement cycles were performed until the final reliability factor was less than 10 %, thereby ensuring sufficient accuracy. The phase compositions of Cr_2AlC, Al_4C_3 and Cr_3C_2 in the coating were estimated at 91 wt.%, 2 wt.% and 7 wt.%, respectively. Thus, the combined arc/sputtering method used in this study was able to fabricate predominantly single-phase Cr_2AlC MAX phase coatings.

Fig. 3 illustrates the surface and cross-sectional morphologies of the Cr_2AlC coatings. In contrast to the Al-based MAX phase coatings produced by arc technology [18], the coatings here exhibited much denser and crack-free microstructures despite the presence of a small number of micro-particles on its surface (Fig. 3a). Furthermore, EDS mapping (Fig. 3b) revealed that most microparticles were rich in Al and poor in Cr, suggesting that these micro-particles were mainly ejected liquid

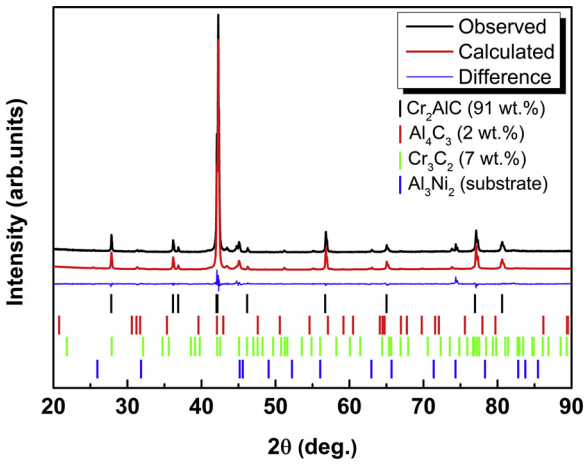

Fig. 2. XRD patterns and Rietveld refinement (calculated) of the as-prepared Cr_2AlC coatings, including identified impurity phases.

droplets from the Al target, which arose because of its low melting point and the high sputtering power applied. The cross-sectional BSE image, along with the EDS line scanning analyses (Fig. 3c) demonstrated that the coatings were dense, homogenous, and strongly adhered. Furthermore, the coatings could be divided into two layers: an inner diffusion layer of ~3.5 μm thickness and a ~10 μm thick outer Cr_2AlC layer. Combined with the EDS line scanning results of the as-prepared Cr_2AlC coatings (Fig. 3c) and as-deposited Cr-Al-C coatings (inserted image in the lower left corner of Fig. 3c), it was apparent that Cr-rich interlayer in the as-deposited Cr-Al-C coatings disappeared and a diffusion layer, composed of Ni, Mo and Al, appeared due to the elemental interdiffusion between substrate and coatings during heat treatment. The strong adherent interface between coating and substrate was clear and relatively sharp, without any defects, such as delamination and cracks. The absence of defects contributed to the oxidation resistance of the coatings at high temperature.

Fig. 4 shows the cross-sectional view TEM and HRTEM micrographs of as-prepared Cr_2AlC coatings. The coating exhibited dense equiaxed crystal structure (Fig. 4a) rather than a columnar crystal structure, as reported in previous studies [19]. This could reduce the short and fast diffusion paths of aluminum or oxygen, conferring the MAX phase coatings high thermal stability [19]. Cr_2AlC has a hexagonal close-packed crystal structure with a space group of $P6_3/mmc$, and the Wyckoff positions were determined to be *4f* for Cr, *2a* for C, and *2d* for Al [20]. The atom stacking sequence of Cr_2AlC along [0001] direction can be identified as ABABAB, where the underlined letters correspond to the Al layer, and other letters refer to the layer of Cr. This stacking sequence emerged clearly in the HRTEM image (Fig. 4b), with the electron beam parallel to the [11–20] direction. The c lattice parameter deduced from the HRTEM image, as indicated in Fig. 4b, was 1.28 nm. Together with the corresponding SAED pattern in Fig. 4c, the lattice parameters of a and c were calculated as 0.286 nm and 1.282 nm, respectively, which agreed well with previous measurements [8].

3.2. Oxidation kinetics

The oxidation kinetics of as-prepared Cr_2AlC coatings were investigated during isothermal oxidation in air for 40 h at 900, 1000 and 1100 °C. The mass gain increased with increasing oxidation temperature (Fig. 5). By plotting the curves as (mass gain/area)^2 versus time (Fig. 5b), the oxidation kinetics could be definitely expressed according to the fitted results. For all three-oxidation temperatures, two linear relationships were apparent and these revealed the two oxidation stages and reflected the parabolic kinetics for each (stage I and stage II). The

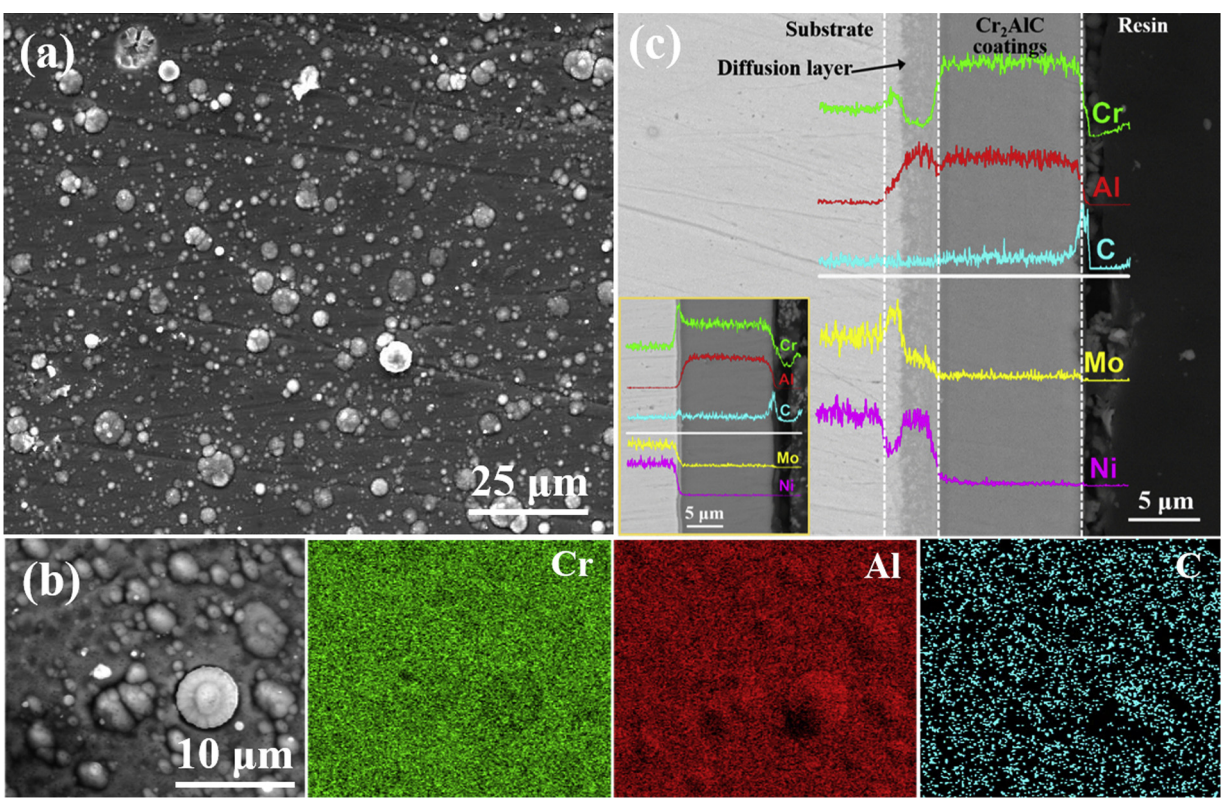

Fig. 3. (a) Surface morphologies of the as-prepared Cr_2AlC coatings. (b) Higher magnification cross-sectional morphologies of the as-prepared Cr_2AlC coatings and corresponding Cr (green), Al (red), and C (blue) elemental maps. The inserted image in the lower left corner represents the same results of as-deposited Cr-Al-C coatings. (c) Cross-sectional morphologies (BSE mode) and corresponding line-scanning of Cr (green), Al (red), C (blue), Mo (yellow), and Ni (magenta) signals along the marked white line. (For interpretation of the references to colour in this figure legend, the reader is referred to the web version of this article).

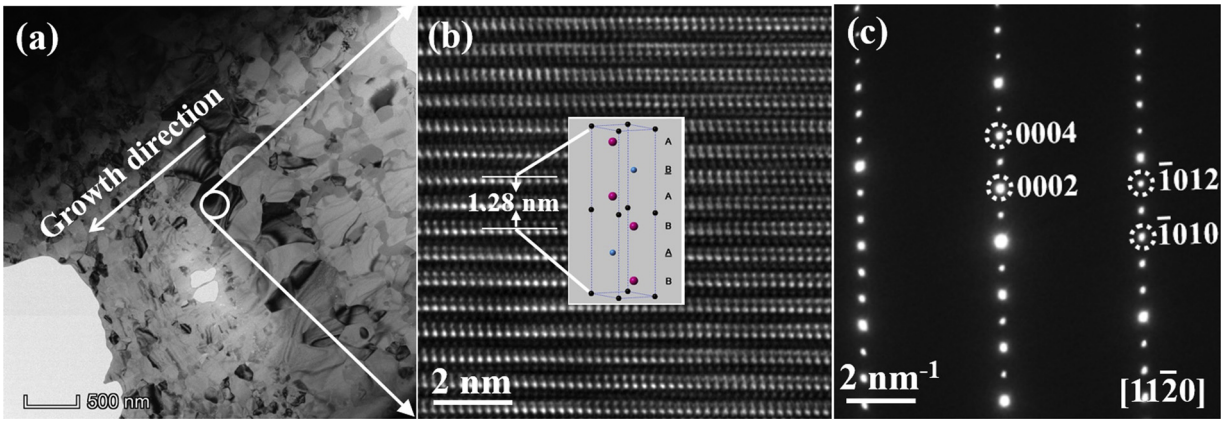

Fig. 4. TEM results of as-prepared Cr_2AlC coatings. (a) TEM bright-field image of the coating at low magnification. (b) HRTEM image of the grain within the round solid line in (a), and the inserted image showing the unit cell of Cr_2AlC. (c) The corresponding SAED with the electron beam parallel to the [11–20] direction.

pattern of parabolic oxidation demonstrated that oxidation was controlled by diffusion throughout the whole reaction [21]. Similar parabolic law has been completely investigated in other reported studies [22–24]. The parabolic rate constant, k_p in mg^2/(cm^4·h), can be calculated from $(\Delta m/A)^2 = k_p t + C$, where Δm is the mass change, A is the surface area, t is the oxidation time, and C is the integration constant [25]. All the fitted rate constants are summarized in Table 1; R^2 values exceeded 0.99, indicating a good fit to the results. However, the rate of mass gain of the Cr_2AlC coatings was larger in stage I than state II because no perfect oxide scale was formed during stage I. In addition, the oxidation kinetics declined relative to the predicted parabolic relationship after ~20 h (stage II) at 1100 °C, generally due to the oxidation/evaporation of Cr_2O_3 [12]. Further discussion of this is given in the next section.

Fig. 6 shows the XRD results of the Cr_2AlC coatings after oxidation tests at different temperatures. Since there were Cr_7C_3, Cr_3C_2 and α-Al_2O_3 peaks in addition to the Cr_2AlC peak in the XRD patterns of the Cr_2AlC coatings oxidized at 900 °C, it could be deduced that Cr_2AlC coatings were not completely oxidized after 40 h oxidation at 900 °C, and they gradually decomposed into Cr_7C_3 and Cr_3C_2 during oxidation. However, coatings oxidized at 1000 and 1100 °C, exhibited the appearance of Cr_2C and Cr_2O_3 phases, and the Cr_2C phase became dominant. Simultaneously, the Cr_2AlC and Cr_3C_2 phases disappeared and the content of Cr_7C_3 decreased significantly. Moreover, the diffraction peak of the Cr_2C phase (Fig. 6b) shifted towards lower 2θ values with increasing oxidation temperatures. This might be attributed to an evolution of a and/or c lattice parameters of the Cr_2C phase, by incorporation of C with N, which will be discussed in the following section.

Table 1
Summary of the parabolic rate constants for the oxidation of Cr_2AlC coatings at 900 – 1100 °C.

Oxidation temperature (°C)	Stage I		Stage II	
	K_p (mg^2/cm^4•h)	R^2	K_p (mg^2/cm^4•h)	R^2
900	1.31×10^{-2}	0.993	2.34×10^{-3}	0.999
1000	1.62×10^{-2}	0.994	7.72×10^{-3}	0.998
1100	1.45×10^{-1}	0.991	2.57×10^{-2}	0.992

3.3. Microstructure evolution: isothermal oxidation at 900 °C

Fig. 7 shows the surface morphologies of Cr_2AlC coatings after 40 h oxidation at 900 °C. Granular oxides were mainly formed on partially localized surface areas and the oxidized coatings still retained a dense structure (Fig. 7a), demonstrating that the oxidation was mild. X-ray diffraction analyses demonstrated that the oxides at 900 °C were mainly composed of α-Al_2O_3, which exhibited good crystallinity at temperatures above 1000 °C. Consequently, it was difficult to establish the presence of α-Al_2O_3 because of the limited resolution of SEM.

To understand the microstructural evolution of Cr_2AlC coatings after 40 h oxidation at 900 °C, cross-sectional SEM measurements for the oxidized coatings were examined. Fig. 8a shows the cross-sectional BSE image and corresponding EDS mapping of the oxidized Cr_2AlC coatings. The microstructure of the Cr_2AlC coatings changed due to oxidation. After 40 h oxidation at 900 °C, a continuous and compact oxide layer was formed on the coating surface. EDS mapping demonstrated that this oxide layer was composed of Al_2O_3. Underneath this

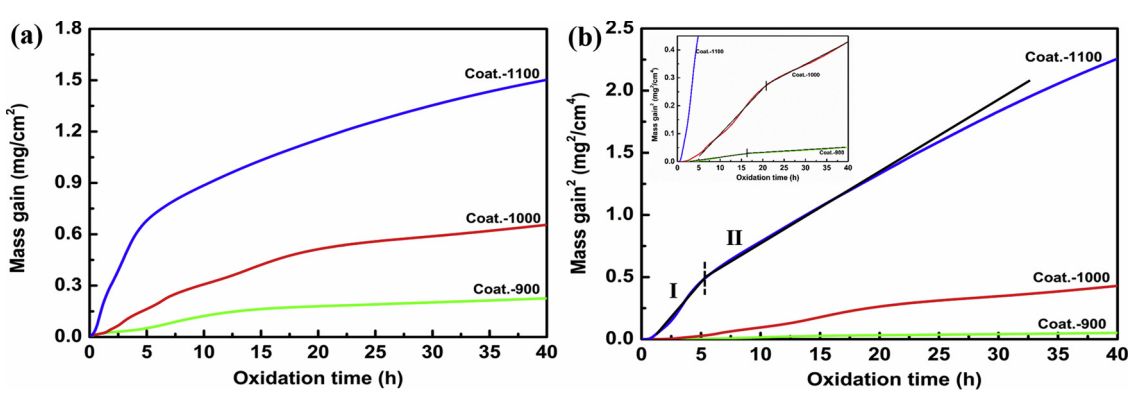

Fig. 5. (a) Mass gain per unit surface area as a function of time. (b) Square of mass gain per unit surface area as a function of time (the inset representing the detail in the initial stage). The vertical dash line and the black line show the dividing point of the oxidation stage and the fitting results of the experimental results, respectively.

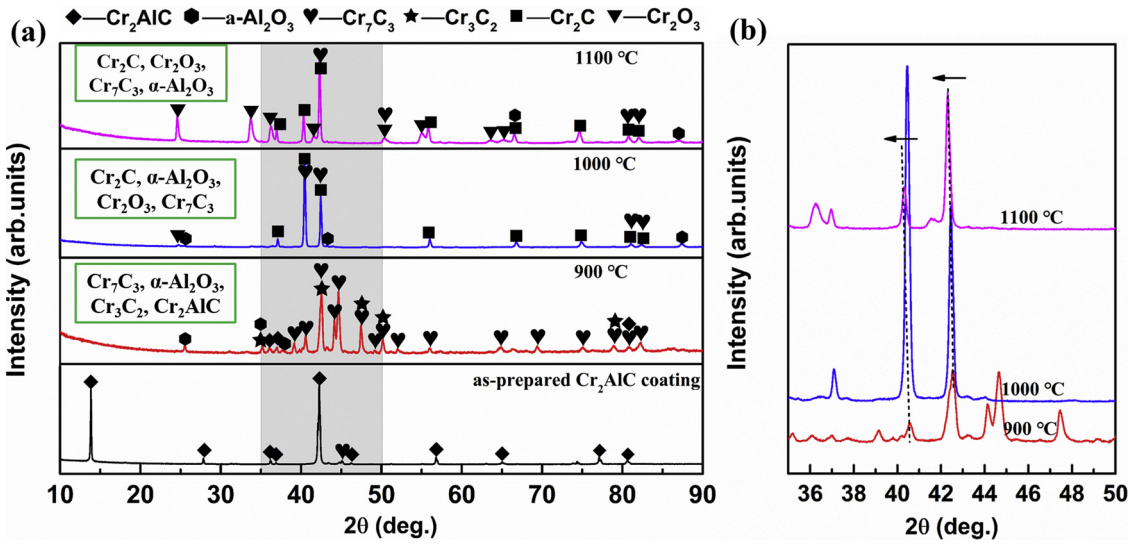

Fig. 6. (a) XRD patterns of the coated samples after oxidation for 40 h at 900 − 1100 °C; (b) enlarged view of the 2θ at 35-51°. The black arrows represent the diffraction peak shift toward low angles.

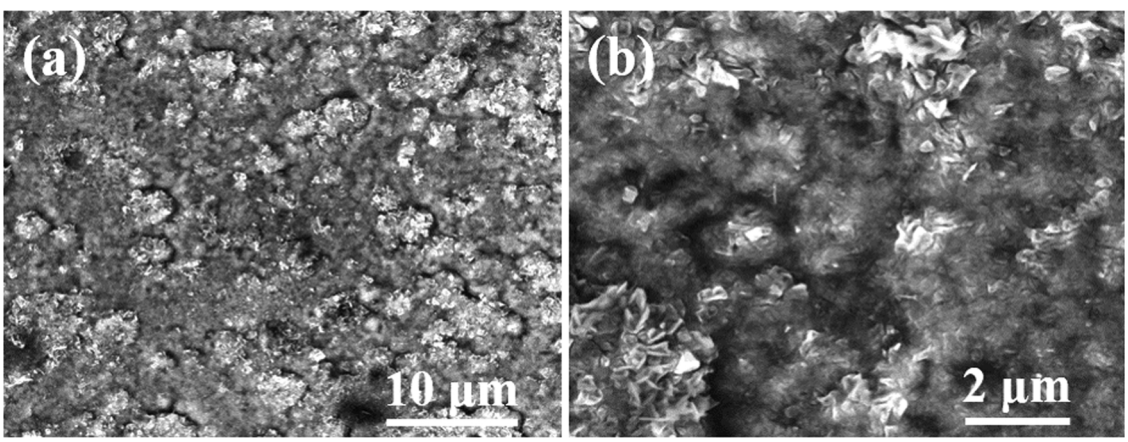

Fig. 7. Surface morphologies of Cr_2AlC coatings after being oxidized for 40 h at 900 °C (a) low magnification and (b) high magnification images.

oxide layer, a loose layer with some voids appeared, due to the external diffusion of Al. This porous layer also contained more oxygen than the compact coating, and many molecules of oxygen had diffused into the inner layer of the coatings though the outer Al_2O_3 layer and this porous layer, leading to the internal oxidation of the coatings. The coating/substrate interface disappeared (Fig. 8a) after oxidation due to the interdiffusion of Cr, Al and Ni between the coating and substrate. Moreover, there were many white precipitate phases distributed unevenly within the substrate. As shown in the EDS mapping, these precipitate phases were confirmed as Mo-rich phases, resulting from the alloying of Mo in the substrate.

The scale formed on the Cr_2AlC coating surface was rich in Al and O, consistent with the EDS mapping (Fig. 8a). To further confirm the thickness and composition of the outmost oxide layer, STEM morphologies and corresponding EDS mapping were analyzed (Fig. 8b). The STEM image reveals the contrast in chemical composition. An intact and well adhered Al_2O_3 layer with a thickness of 220 nm was formed on the surface (Fig. 8b), while Cr_2O_3 oxide was not visible within this layer at 900 °C, consistent with the XRD results. Beneath the Al_2O_3 scale, a Cr-rich carbide layer was clearly apparent, resulting from the inter-diffusion of Al and the decomposition of the Cr_2AlC MAX phase during oxidation. Furthermore, oxygen could also be detected within this Cr-rich layer, and few Al-rich oxide precipitates appeared in the cross-sections of oxidized coatings, as indicated by the white arrows in Fig. 8b. These precipitates might reflect the internal Al_2O_3 oxides, which formed as a result of the inward diffusion of oxygen through the thin Al_2O_3 layer.

Transmission electron microscopy analyses were performed to examine the formation of carbide compounds. A typical EDS spectrum of Cr_7C_3 phase is presented in Fig. 9a. Chromium, carbon and Cu were detected, while Cu was mainly derived from the TEM grid. The SAED pattern (Fig. 9b) indicated that Cr_7C_3 was present in the oxidized sample. Transmission electron microscopy analyses suggested that the direction of the electron beam was parallel to the [010] plane of the orthorhombic Cr_7C_3. The corresponding fast Fourier transformation pattern from a typical HRTEM pattern of Cr_7C_3, further demonstrated the formation of the Cr_7C_3 phase after oxidation (Fig. 9c). In addition, the EDS spectrum of Cr_3C_2 was also apparent (Fig. 9d). A typical SAED image of orthorhombic Cr_3C_2, recorded with the electron beam parallel to [−111] zone axis, is displayed in Fig. 9e, and Fig. 9f shows the corresponding fast Fourier transformation pattern of Cr_3C_2. Combined with the results from XRD and TEM, the presence of oxidation products, including Cr_7C_3 and Cr_3C_2, as well as α-Al_2O_3 was identified.

3.4. Microstructure evolution: isothermal oxidation at 1000 °C

Morphologies of the Cr_2AlC coatings after 40 h oxidation at 1000 °C are presented in Fig. 10. In contrast to the oxidation at 900 °C, the oxidized coatings at 1000 °C were composed of compact oxides with fine grains (Fig.10a), and the oxides were clearly apparent on the

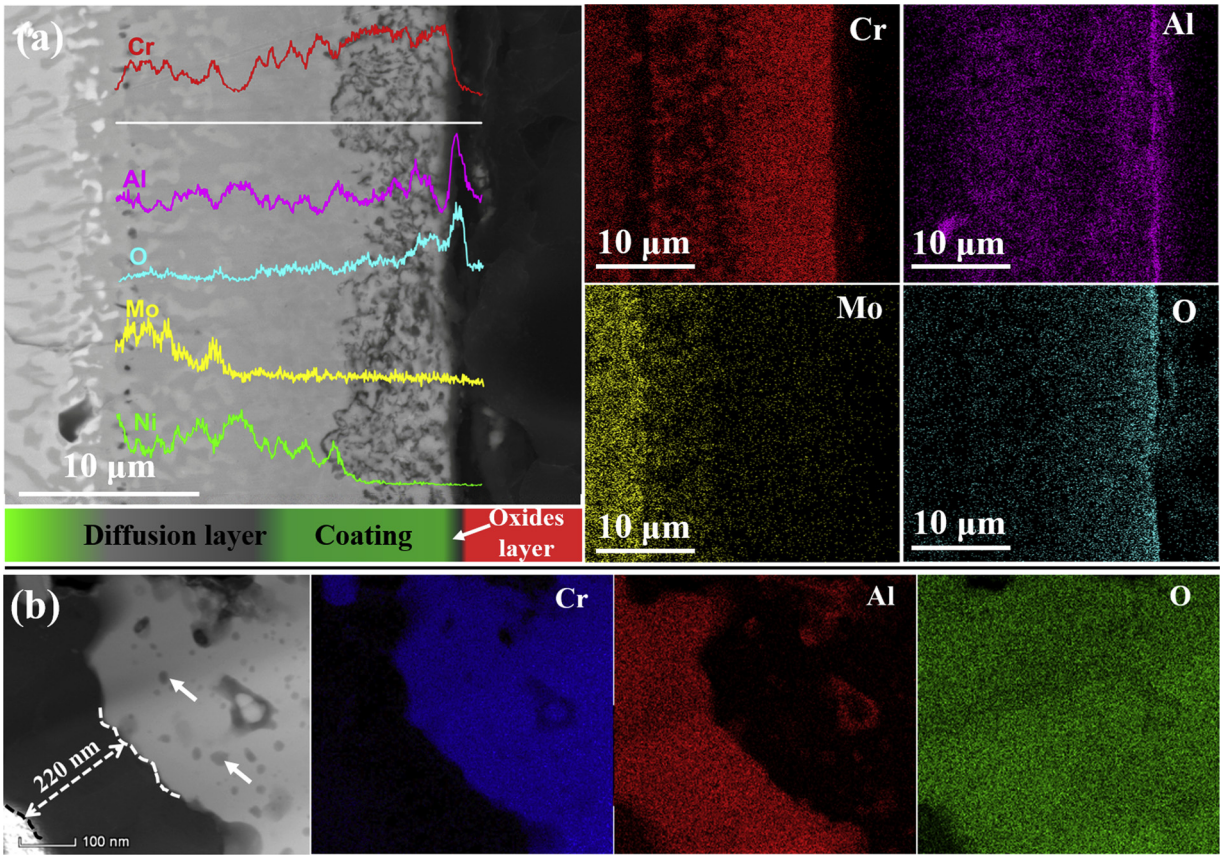

Fig. 8. (a) Cross-sectional SEM micrographs of the oxidized Cr_2AlC coatings at 900 °C for 40 h, corresponding line-scanning profiles of Cr, Al, O, Mo and Ni elements along the white solid line, and Cr (red), Al (magenta), Mo (yellow) and O (sky-blue) elemental maps. (b) Cross-sectional STEM micrographs with Cr (blue), Al (red) and O (green) elemental maps of the outmost oxide layer for the oxidized Cr_2AlC coatings. (For interpretation of the references to colour in this figure legend, the reader is referred to the web version of this article).

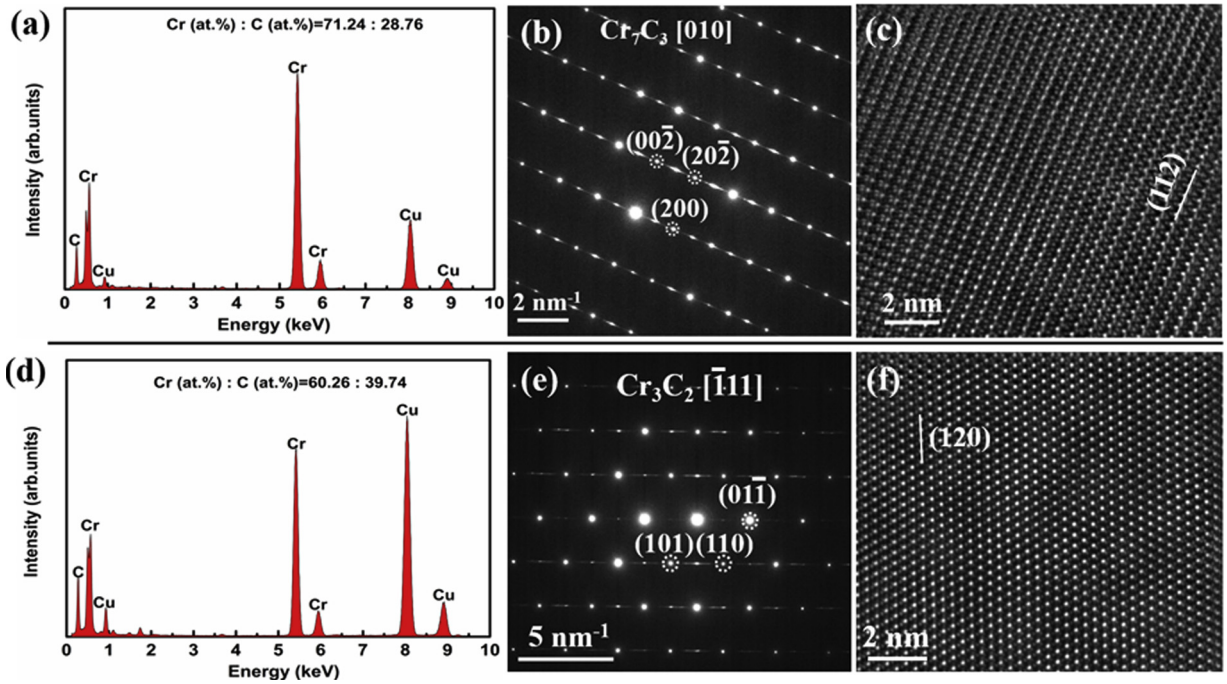

Fig. 9. (a) EDS profile for the formed Cr_7C_3 after oxidation at 900 °C for 40 h; (b) corresponding SAED patterns with the electron beam parallel to the [010] zone axis; and (c) HRTEM bright-field image; (d) EDS profile for the formed Cr_3C_2 after oxidation at 900 °C for 40 h. (e) Corresponding SAED patterns with the electron beam parallel to the [-111] zone axis, and (f) HRTEM bright-field image.

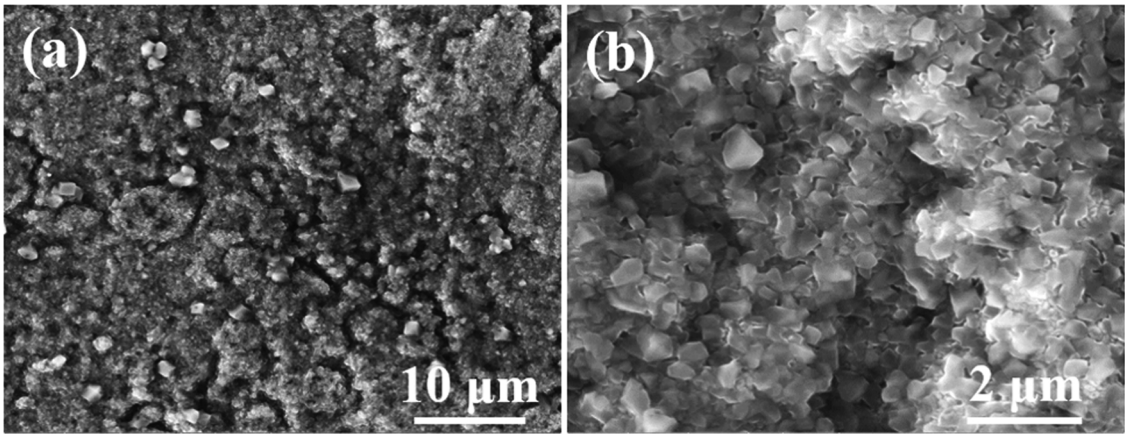

Fig. 10. Surface morphologies of the oxidized Cr_2AlC coatings at 1000 °C for 40 h, (a) low magnification image and (b) high-magnification images.

coating surface. The grain sizes of the oxides were larger compared to those at 900 °C (Fig. 10b), probably because of the formation of Cr_2O_3, as confirmed by the XRD results. No cracks or spallation of the oxide scale were found and no needle-like metastable alumina morphology was visible on the coating surface, indicating that no θ-Al_2O_3 was formed after oxidation, consistent with the XRD results.

The cross-sectional morphologies of the Cr_2AlC coatings after 40 h oxidation at 1000 °C are presented in Fig. 11. A compact and continuous oxide layer 390 nm thick was formed on the coating surface (Fig. 11a). Further examination using STEM (Fig. 11b) of this outer oxide layer suggested that it was composed of mixed oxides, including Al_2O_3 and Cr_2O_3, which differed from the layer generated at 900 °C. This is responsible for the oxidation of strong Cr-C covalent bonds in the Cr_2AlC MAX phase, thereby restricting the activity of Cr at 900 °C. Hexagonal Cr_2O_3 and α-Al_2O_3 could form the $(Al, Cr)_2O_3$ solid solution phase at temperatures exceeding 950 °C over the entire compositional range, as noted previously by several authors, in the scale of oxidized Cr_2AlC [26] and Al_2O_3 forming alloys containing Cr [27]. In addition, granular precipitates at the coating/substrate interface were found but they did not form a continuous layer. Results of the EDS analyzes demonstrated that these precipitates were mainly consisted of Al, consistent with the high activity of Al in Cr_2AlC MAX phase, which allowed

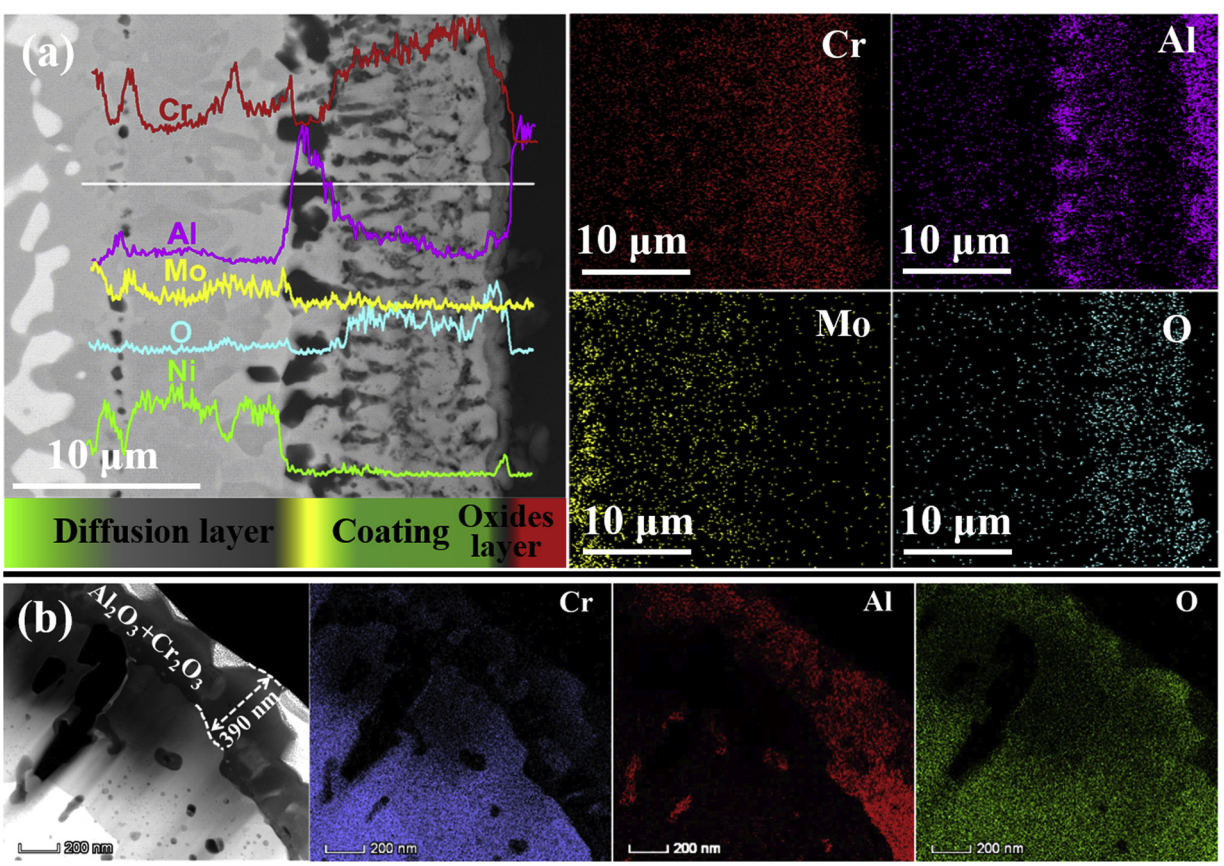

Fig. 11. (a) Cross-sectional SEM micrographs of the oxidized Cr_2AlC coatings at 1000 °C for 40 h, corresponding line-scanning profiles of Cr, Al, O, Mo and Ni elements along the white solid line, and Cr (red), Al (magenta), Mo (yellow) and O (sky-blue) elemental maps. (b) Cross-sectional STEM micrographs with Cr (blue), Al (red) and O (green) elemental maps of the outmost oxide layer for oxidized Cr_2AlC coatings. (For interpretation of the references to colour in this figure legend, the reader is referred to the web version of this article).

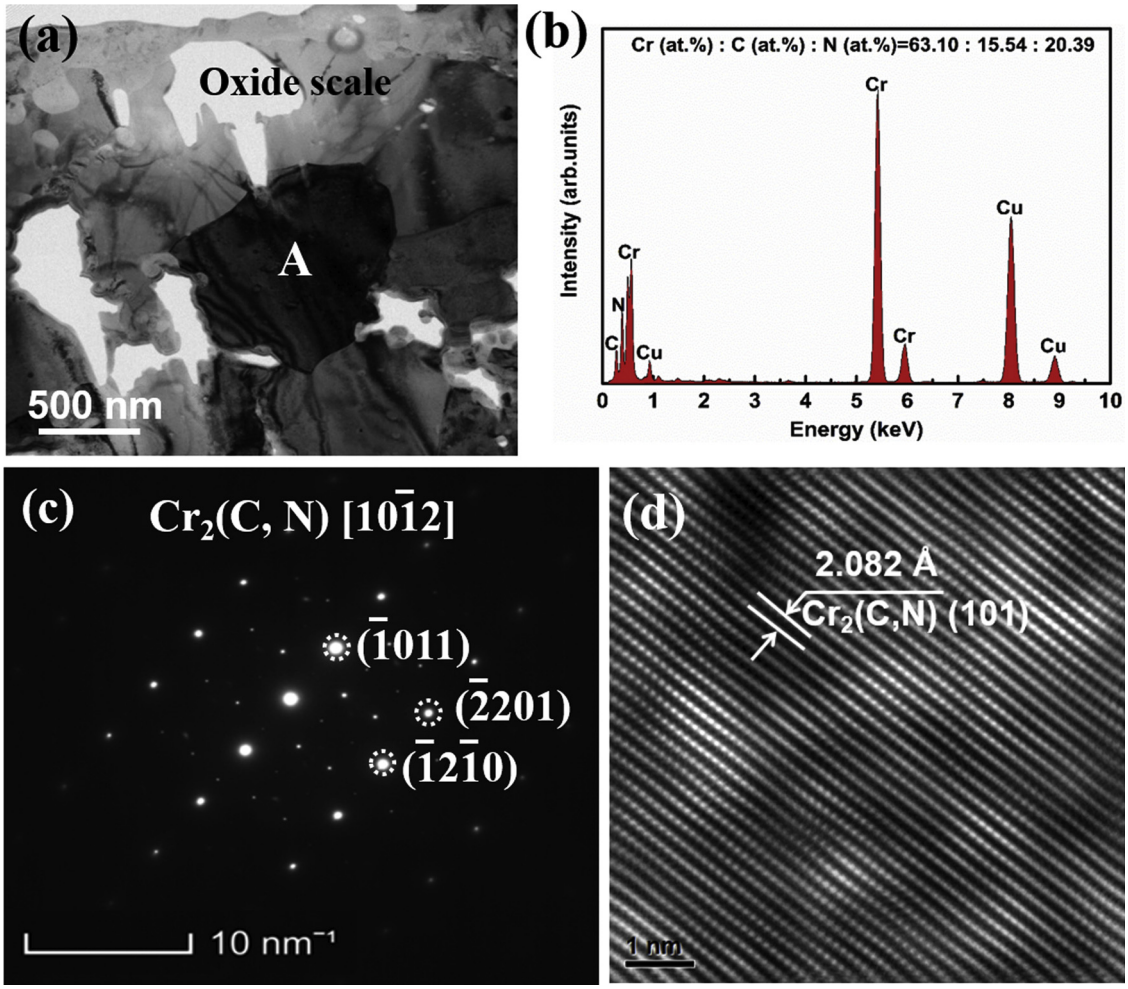

Fig. 12. (a) Low magnification TEM bright-field image of the oxidized coating at 1000 °C for 40 h. (b) EDS profile for the formed $Cr_2(C, N)$ grain labeled as "A" in (a); (c) corresponding SAED patterns with the electron beam parallel to the [10–12] zone axis; and (d) HRTEM bright-field image.

Al in the coating to diffuse faster to the substrate, resulting in an enrichment of Al at the interface. After 40 h oxidation at 1000 °C, there was minimal Al within the coating (Fig. 11), which means that a significant fraction of the Cr_2AlC MAX phase was consumed during oxidation. Meanwhile, a large amount of oxygen was detected within the coating as a result of internal oxidation, leading to the formation of many Al_2O_3 precipitates underneath the oxide scale. The outward diffusion of Cr, Mo and Ni cannot occur at 1000 °C due to the higher internal diffusion of Al to the interface.

To further clarify the mechanism of oxidation of Cr_2AlC coatings at 1000 °C, TEM analysis of the carbide was conducted and the results are shown in Fig. 12. Unexpectedly, EDS analysis of the selected region (marked in Fig. 12a as "A") demonstrated that nitrogen was present as this was not true for samples oxidized at 900 °C. Thus, the carbide corresponding to Cr_7C_3 and Cr_3C_2 changed to $Cr_2(C, N)$ when the oxidation temperature increased from 900 °C to 1000 °C. Thermodynamic calculations revealed that Cr_2N is also a thermodynamically stable phase when N is present and thus the nitridation reaction may start after oxidation. Hence the internal nitridation phases can be formed beneath the outmost oxide scale in regions possessing carbides. Nitridation was observed on the Cr_2AlC coatings during oxidation in air by Li et al. [12], where the AlN phase appeared at the interface of the coating and substrate after oxidation at 1000 °C and 1100 °C. A SAED pattern from the selected area is shown in Fig. 12c. The pattern can be indexed to Cr_2C (hexagonal crystal system, space group: -3 m) having lattice parameters of a = 0.28 nm and c = 0.59 nm. The larger c value, compared with the standard lattice parameters, was probably due to the behavior of nitridation. The electron beam was parallel to the [10$\bar{1}$2] direction of the hexagonal Cr_2C. Previous studies have reported that a small amount of N could replace C in the Cr_2C to form $Cr_2(C, N)$, resulting in changes to the lattice parameters and a lower shift of diffraction angle (2θ), as determined by XRD analysis. Fig. 12d shows the HRTEM image of area "A", which further indicated that the planar spacing of 2.08 Å was corresponded to the (101) orientations of hexagonal Cr_2C, but this was slightly lower than the constant of Cr_2C without nitridation. Similar shrinkage of metal carbide caused by partitioning of nitrogen has also been reported previously [28]. Therefore, the measured shrinkage in planar spacing is an indication of partial nitrogen replacement in Cr_2C to form the $Cr_2(C, N)$ solid solution.

3.5. Microstructure evolution: isothermal oxidation at 1100 °C

Fig. 13 shows the surface morphologies of the Cr_2AlC coatings after 40 h oxidation at 1100 °C. At this higher temperature, oxidation became more severe, but no cracks and spallation occurred on the coating surface. As expected, the oxidized coating surface become loose compared to that at 900 °C or 1000 °C and multiple holes were visible. This arose because when the oxidation temperature increased to 1100 °C, Cr_2O_3 oxides changed to gaseous CrO_3, leading to many holes on the surface [12]. Additionally, the oxide grain changed from a granular structure to a cauliflower-like structure, and grain size declined, which was likely related to variations in the composition of the oxides.

The morphologies of oxide scale after 40 h oxidation at 1100 °C are presented in Fig. 14. A compact and continuous oxide layers was

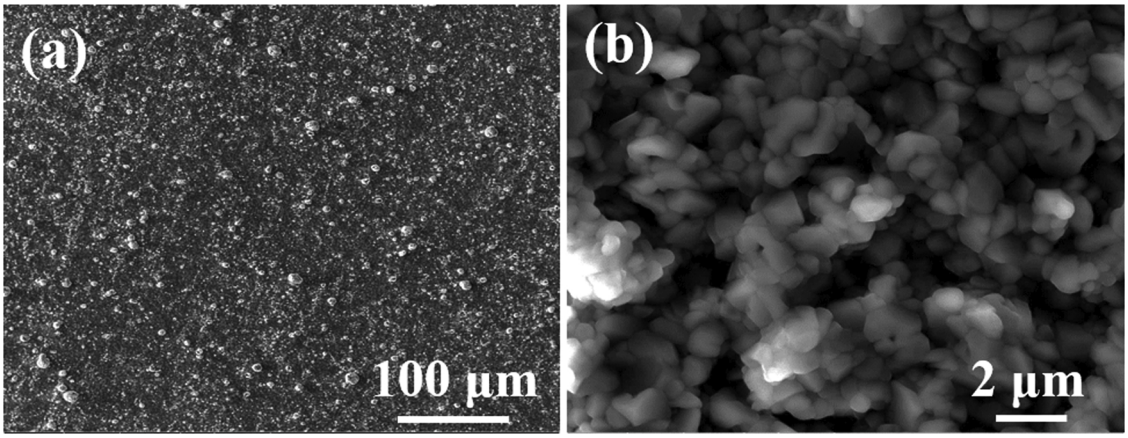

Fig. 13. Surface morphologies of the oxidized Cr_2AlC coatings at 1100 °C for 40 h. (a) Low magnification image, and (b) high-magnification image.

formed on the coating surface, as revealed through cross-sectional BSE imagery and corresponding EDS analysis (Fig. 14a). The outer layer was composed of mixed oxides of Al_2O_3 and Cr_2O_3, as confirmed by the EDS line scanning and EDS mapping results, similar to observations of the oxide layer at 1000 °C. A closer examination of the outer scale (Fig. 14b) revealed that the scale became thicker (~780 nm) and the content of Cr_2O_3 oxides increased with increased oxidation temperature. Furthermore, a thin Al_2O_3 oxide layer appeared between the coating and substrate, which would provide significant protection against further oxidation of the substrate and act as a diffusion barrier to retard elemental inter-diffusion. This phenomenon has been previously observed in MCrAlY coatings [29], after the oxidation of Al under a low oxygen partial pressure. Rastegari et al. [30] reported that a thin α-Al_2O_3 layer fabricated by the electron beam PVD (EB-PVD) can successfully block diffusion of substrate alloy elements, including Mo, W, into the coating. The EDS results demonstrated the presence of Mo in the coating, indicating that the majority of Mo diffused into the coating before the formation of the continuous Al_2O_3 layer. This could be attributed to a large concentration difference and the tendency for the formation of volatile MoO_3 at temperatures exceeding 1100 °C, as reported by other researchers [31]. In addition, EDS results suggested that the O content beneath the coating surface corresponded, approximately, to internal oxidation, and internal oxidation within the coating mainly resulted in the formation of alumina, which exhibits a darker

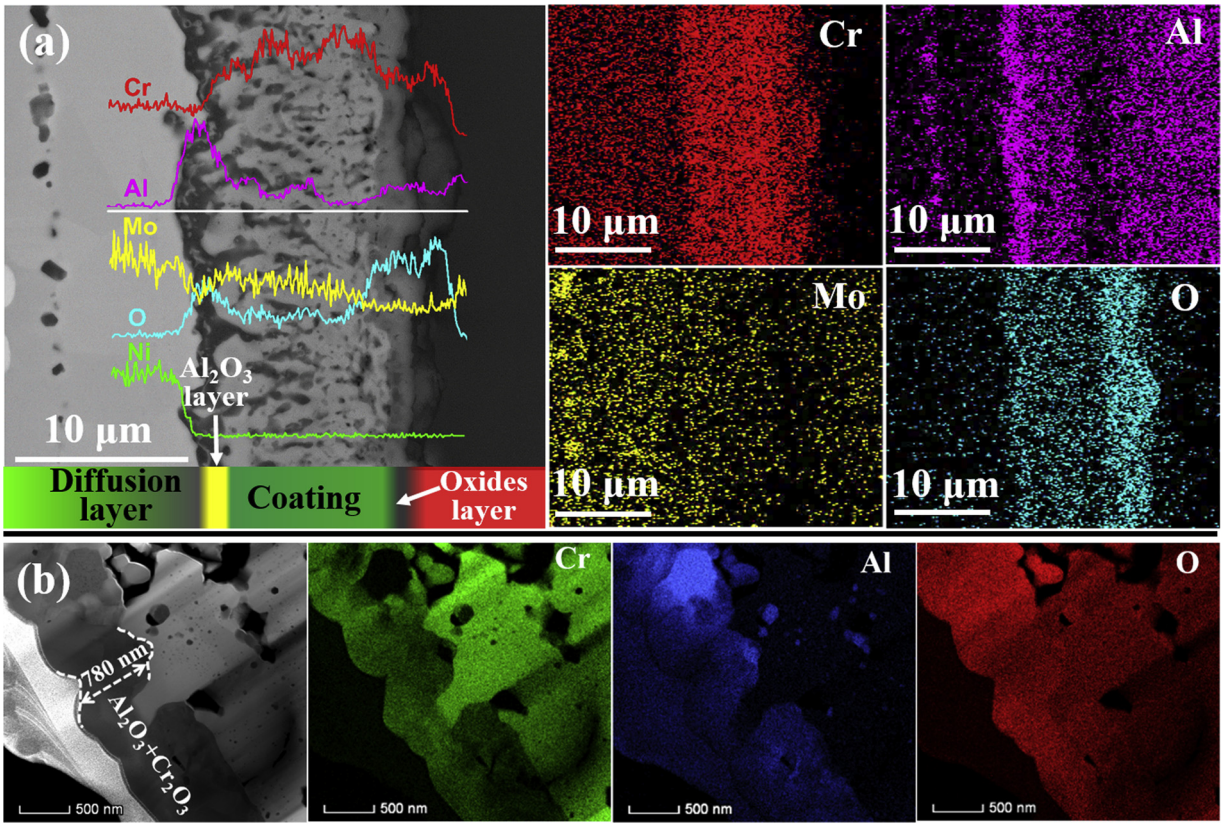

Fig. 14. (a) Cross-sectional SEM micrographs of the oxidized Cr_2AlC coatings at 1100 °C for 40 h, corresponding line-scanning profiles of Cr, Al, O, Mo and Ni elements along the white solid line, and Cr (red), Al (magenta), Mo (yellow) and O (sky-blue) elemental maps. (b) Cross-sectional STEM micrographs with Cr (green), Al (blue) and O (red) elemental maps of the outmost oxide layer for this oxidized Cr_2AlC coatings. (For interpretation of the references to colour in this figure legend, the reader is referred to the web version of this article).

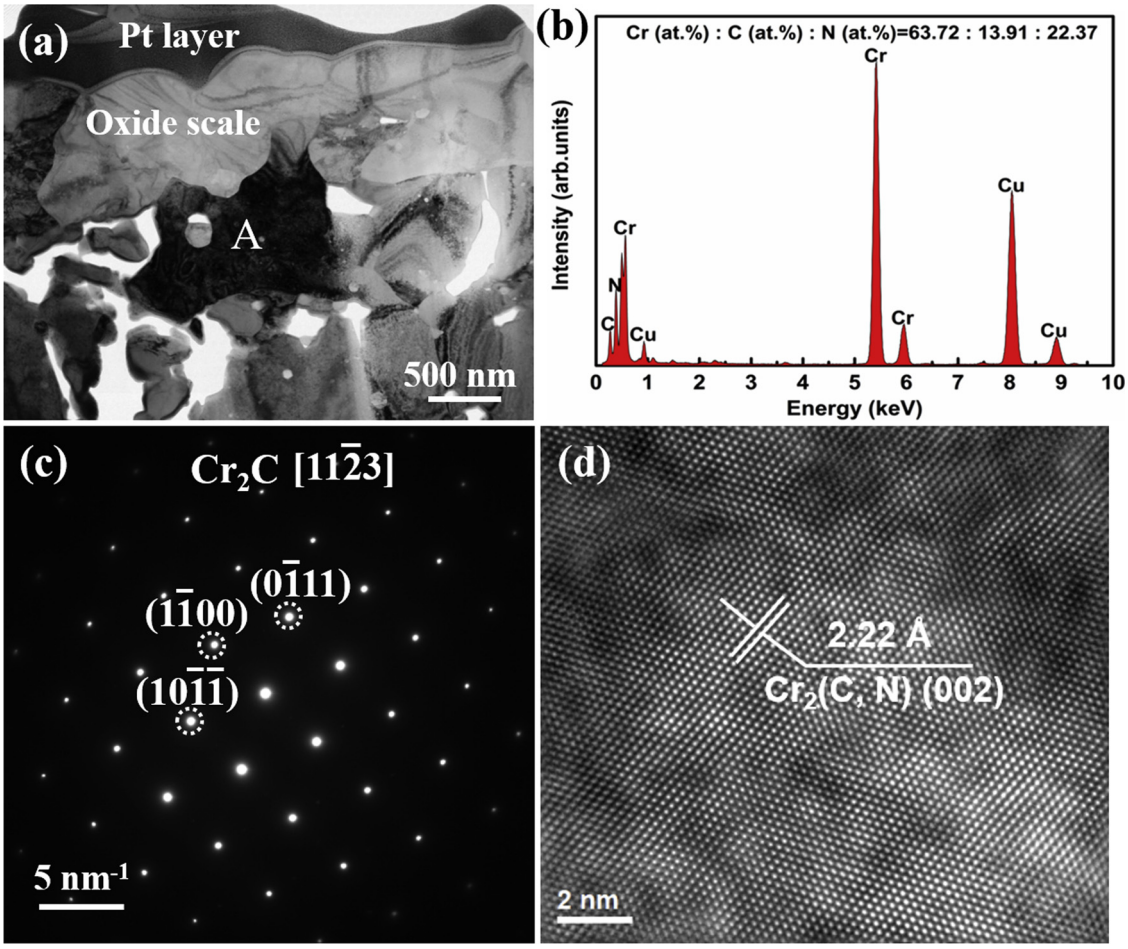

Fig. 15. (a) Low magnification TEM bright-field image of the oxidized coating at 1100 °C for 40 h. (b) EDS profile of the $Cr_2(C, N)$ grain labeled as "A" in (a); (c) corresponding SAED patterns with the electron beam parallel to the [11–23] zone axis; and (d) HRTEM bright-field image.

contrast in Fig. 14a.

Fig. 15 displays the TEM results of the carbide produced after 40 h oxidation at 1100 °C. As observed after oxidation at 1000 °C, EDS results of the selected region (marked in Fig. 15a as "A") in Fig.15b demonstrated that this carbide contained some nitrogen, indicating that internal nitridation also occurred at 1100 °C. The SAED pattern of the area marked as "A" revealed that the grain was a hexagonal Cr_2C, with lattice parameters of a = 0.26 nm and c = 0.51 nm, which deviated little from the standard lattice constant due to nitridation. HRTEM further confirmed that Cr_2C possessed a representative crystal plane of (002) and a lattice spacing of 2.22 Å (Fig. 15d).

The dense and continuous Al_2O_3 interfacial layer produced during oxidation at 1100 °C could play a key role in further improving the oxidation resistance of coatings and act as a diffusion barrier. The HRTEM results of the Al_2O_3 layer (labeled as area#1 in Fig. 16a) and corresponding SAED (Fig. 16b and c) confirmed that the Al_2O_3 had the hexagonal close-packed (hcp) crystal structure of α-Al_2O_3. In addition, the interfaces of α-Al_2O_3/substrate and α-Al_2O_3/coatings exhibited coherent epitaxial growth without dislocation, despite the large lattice mismatches, and thus might render the oxidized coatings considerable strong adhesion to the substrates. Indeed, damage arising from thermal stress, leading to spalling failure, is one of the most critical damage modes for high temperature coatings. Thermal shock tests of the oxidized coatings at 1100 °C demonstrated that the oxidized coatings were still firmly bonded to the substrates, with the except that exfoliation of the outermost oxide layer occurred after 60 cycles of thermal shock tests.

4. Discussion

At an oxidation temperature of 900 °C, scales of the oxidized Cr_2AlC coatings were composed of an outer Al_2O_3 layer and an inner mixed Cr-C layer. However, the appearance of Cr-C phases, including Cr_3C_2 and Cr_7C_3, rather than Cr_2O_3 in the inner layer of the oxidized coatings, revealed that Cr_2AlC beneath the surface Al_2O_3 oxide scale was mainly transformed to carbides.

Thermodynamically, the Gibbs energies of the formation of Cr_2O_3 and Al_2O_3 were −827.99 kJ/mol and −1303.57 kJ/mol, respectively; thus Al_2O_3 was more easily formed than Cr_2O_3. Consequently, when Al and Cr coexisted and kinetic conditions were satisfied, Al_2O_3 is preferentially formed. Moreover, both theory and experiments demonstrated that Al in Cr_2AlC MAX phases has a high rate of diffusion and activity at high temperatures, resulting from its layered hexagonal structure with CrC-groups separated by pure elemental Al layers [32,33]. Thus, it is proposed that the oxidation of Cr_2AlC coatings at 900 °C resulted from the inward diffusion of O and outward diffusion of Al to form a pure Al_2O_3 phase on the surface layer, while the remaining Cr-C products, Cr_3C_2 and Cr_7C_3, were in the inner layer. Interestingly, no chromium oxides were visible in the XRD results (Fig. 6). Because Cr atoms in Cr_2AlC are bound to carbon atoms by strong covalent and ionic bonding, this strong Cr-C interaction decreases the oxygen affinity of Cr. Hence, aluminum could be oxidized selectively in Cr_2AlC. Accordingly, regardless of the formation of any intermediates, the Cr_2AlC coatings were oxidized and finally converted into Al_2O_3, Cr_7C_3 and Cr_3C_2 in accordance with Eq. (1):

$$20Cr_2AlC + 15O_2 = 10Al_2O_3 + 4Cr_7C_3 + 4Cr_3C_2 \quad (1)$$

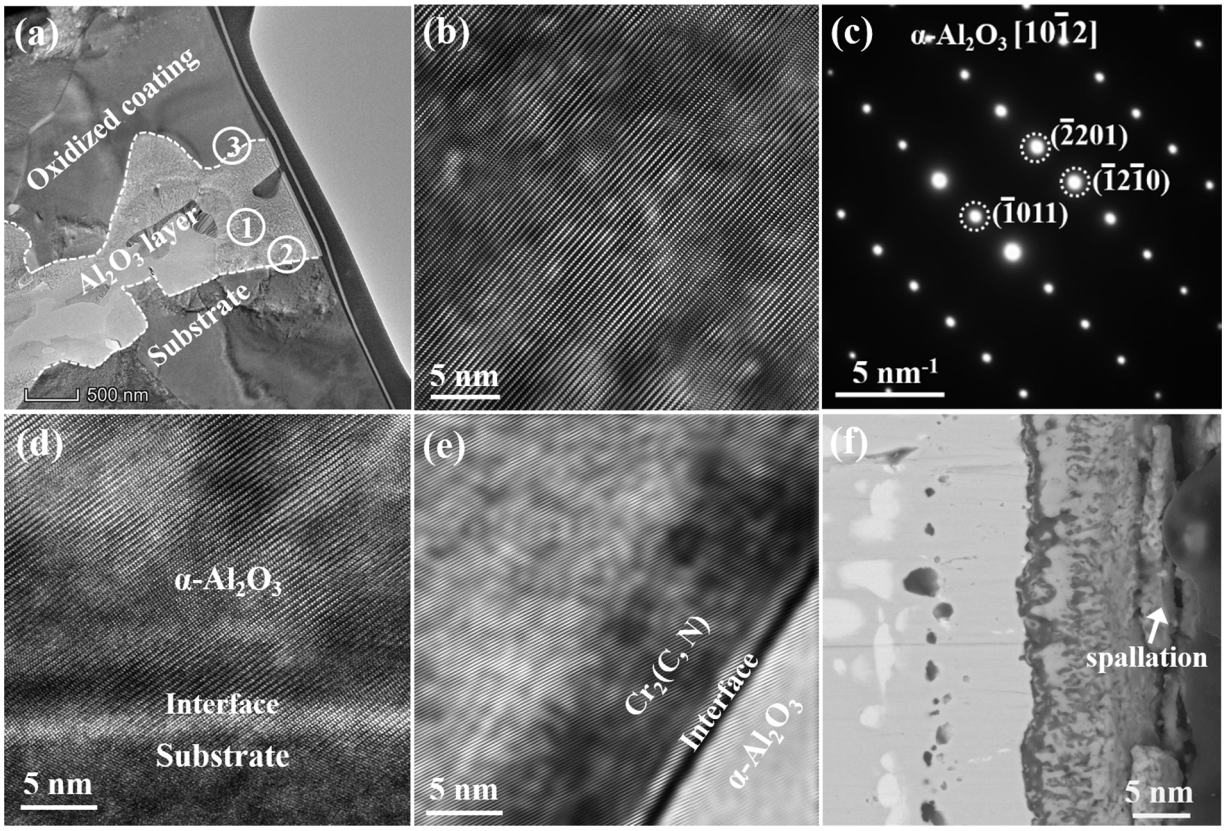

Fig. 16. (a) Low magnification TEM bright-field image of the Al_2O_3 interfacial layer between oxidized coatings at 1100 °C and substrate. (b) HRTEM image of the area#1 in.(a); (c) corresponding SAED patterns with the electron beam parallel to the [10–12] zone axis. (d) HRTEM image of area#2 in. (a). (e) HRTEM image of area#3 in. (a). Cross-sectional morphologies of the oxidized coatings after 60 cycles of thermal shock.

When the oxidation temperature increased to 1000 °C and 1100 °C, a large amount of Al became more active and diffused more rapidly during oxidation, and therefore Al in the Cr_2AlC coatings underneath the oxide scale became depleted. As long as Al was present, the local oxygen partial pressure would remain below 10^{-20} Pa, but once the Al supply was depleted the oxygen partial pressure started to increase and the Cr-carbide phases were oxidized to Cr_2O_3 and Cr_2C, as indicated in reaction (2). In addition, Cr_2C could be further oxidized to become Cr_2O_3 and CO_2 or CO (for brevity, only noted as CO), according to reaction (3). The formed Cr_2O_3 could then react with Al_2O_3 to form a $(Cr, Al)_2O_3$ solid solution layer, as reported in previous studies [34,35]. However, in this work, $Cr_2(C, N)$, not Cr_2C, was identified underneath the oxide scale after oxidation at 1000 °C and 1100 °C, suggesting that nitrogen could penetrate the coating through the oxide scale to form the $Cr_2(C, N)$ phase. Structural analysis of the oxidized coating (Figs. 11 and 14) demonstrated that the internal oxidation of the Cr_2AlC coatings occurred because of the inward diffusion of oxygen through the oxide scale. Thus, nitrogen in air could also diffuse inwardly through the oxide scale, and then reacted with Cr_2C in the coating to form Cr_2N at the Cr-C region (formula (4)). The latter leads to the formation of $Cr_2(C, N)$ solid solution, because the Cr_2C and Cr_2N have a similar trigonal crystal structure with group space p − 3 m [36]. No Cr carbonitride was detected in the Cr_2AlC coatings at the oxidation temperature of 900 °C nor in the work of Berger et al. [37,38]. It is reasonable to propose that the absence of nitridation is ascribed to low oxidation temperature or short oxidation time.

$$4Cr_7C_3 + 3O_2 = 2Cr_2O_3 + 12Cr_2C \quad (2)$$

$$Cr_2C + 2O_2 = Cr_2O_3 + CO\uparrow \quad (3)$$

$$2Cr_2C + N_2 + O_2 = 2Cr_2N + 2CO\uparrow \quad (4)$$

At temperatures exceeding 1000 °C in air, Cr_2O_3 is not stable, and easily evaporates as CrO_3, as formula (5) shows, resulting in the decline of the oxidation kinetics after approximately 25 h oxidation at 1100 °C. Similar behavior has also been reported during the oxidation of Cr_2AlC coatings and bulk materials [12,39]. Moreover, the consumption of Al at 1100 °C is much more serious than that at 900 °C and 1000 °C, leading to the thicker Cr–C layer, and more Cr in the Cr–C layer is oxidized and finally evaporates as CrO_3.

$$2Cr_2O_3 + 3O_2 = 4CrO_3\uparrow \quad (5)$$

At the oxidation temperatures of 1000 °C and 1100 °C, the consumption of Al was more serious, promoting the formation of a thicker Cr-C layer, thereby hindering the outward diffusion of Al through the Cr-C layer. The enrichment of Al at the coating/substrate interface occurred after oxidation at 1000 °C, which was ascribed to the difference of diffusion rates of Al between the coating/substrate interface and coating surface. The diffusion rate of Al inward to the coating/substrate interface was higher than that of Al outward through the Cr-C layer, resulting in the formation of an Al-rich layer (Fig. 11). Once a continuous scale formed the oxygen partial pressure beneath the oxide scale would be low. In addition, the thickness of the oxide scale at 1100 °C was larger than that at 1000 °C. The higher Al diffusion activity and the lower oxygen partial pressure would promote the formation of a continuous α-Al_2O_3 oxide layer at the coating/substrate interface (Fig.14). Furthermore, α-Al_2O_3 exhibited coherent epitaxial growth with the oxidized coatings and substrates, and then rendered the oxidized coatings with considerable strong adhesion with substrates. Finally, the dense double-layered scales, consisting of one $(Al, Cr)_2O_3$ outermost layer and one α-Al_2O_3 innermost layer, endowed the Cr_2AlC coatings with excellent protection of the substrate alloy during high-temperature oxidation. The process of oxidation is detailed in Fig. 17.

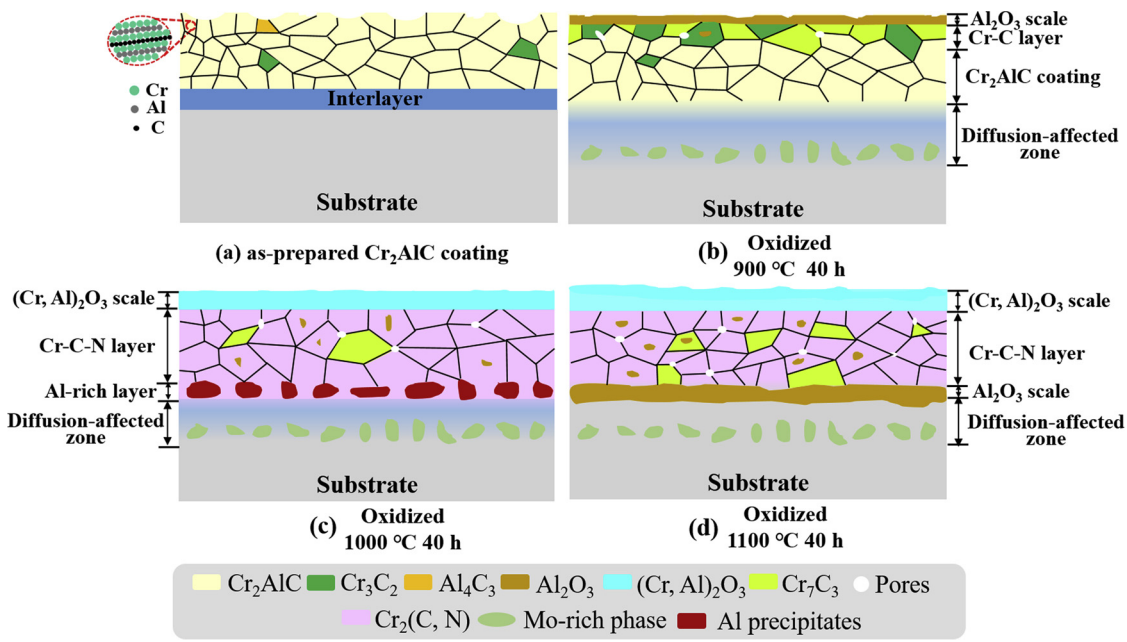

Fig. 17. Schematic diagram of the oxidation mechanism for the Cr_2AlC coatings at different temperatures: (a) as-prepared Cr_2AlC coatings, (b) 900 °C, (c) 1000 °C, (d) 1100 °C.

5. Conclusions

(1) Dense Cr_2AlC MAX phase coatings (purity: 91 wt.%) were successfully prepared on Hastelloy substrates by a novel combined arc/sputtering deposition method, followed by subsequent vacuum annealing. These coatings were free of columnar structures, and consisted of an inner layer (~3.5 μm) and an outer Cr_2AlC layer (~10 μm).

(2) Detailed investigations of the oxidation behavior of the Cr_2AlC coatings at 900 – 1100 °C demonstrated that oxidation kinetics followed a parabolic relationship at each temperature. This relationship could be divided into two stages and the second stage exhibited a slightly lower rate of oxidation.

(3) Structural analysis of the oxidized Cr_2AlC coatings demonstrated that the oxides and carbides formed after 40 h oxidation were significantly affected by oxidation temperature. At 900 °C, a compact and continuous Al_2O_3 outmost layer was produced due to the selective oxidation of Al. This oxidation-induced depletion of Al resulted in the transformation of Cr_2AlC to Cr_7C_3 and Cr_3C_2 phases. A mixed oxide layer composed of Cr_2O_3 and Al_2O_3 was identified at 1000 °C and 1100 °C in addition to the formation of Cr_7C_3 and $Cr_2(C, N)$.

(4) The enrichment of Al occurred at the coating/substrate interface after 40 h oxidation at 1000 °C. The Al-rich interface layer was transformed to a dense α-Al_2O_3 layer when oxidation temperature increased to 1100 °C, further improving the oxidation resistant properties of Cr_2AlC MAX phase coatings.

Data availability

The data that support the findings of this study are available from the corresponding author upon reasonable request.

CRediT authorship contribution statement

Zhenyu Wang: Conceptualization, Methodology, Data curation, Writing - original draft. **Guanshui Ma:** Validation, Writing - review & editing. **Linlin Liu:** Resources, Visualization, Data curation. **Li Wang:** Formal analysis, Investigation. **Peiling Ke:** Project administration, Writing - review & editing, Supervision. **Qunji Xue:** Project administration, Writing - review & editing, Supervision. **Aiying Wang:** Writing - review & editing, Supervision.

Declaration of Competing Interest

The authors declare that they have no known competing financial interests or personal relationships that could have appeared to influence the work reported in this paper.

Acknowledgements

This research was supported by the National Science and Technology Major Project (2017-VII-0012-0108), National Natural Science Foundation of China (51875555, 51901238), and Zhejiang Provincial Natural Science Foundation (LQ19E010002).

Appendix A. Supplementary data

Supplementary material related to this article can be found, in the online version, at doi:https://doi.org/10.1016/j.corsci.2020.108492.

References

[1] M.W. Barsoum, The $M_{n+1}AX_n$phases: a new class of solids: thermodynamically stable nanolaminates, Prog. Solid State Ch. 28 (2000) 201–281.
[2] W.-B. Tian, P.-L. Wang, G.-J. Zhang, Y.-M. Kan, Y.-X. Li, Mechanical properties of Cr_2AlC ceramics, J. Am. Ceram. Soc. 90 (2007) 1663–1666.
[3] T. Go, Y.J. Sohn, G. Mauer, R. Vaßen, J. Gonzalez-Julian, Cold spray deposition of Cr_2AlC MAX phase for coatings and bond-coat layers, J. Eur. Ceram. Soc. 39 (2019) 860–867.
[4] M. Sokol, J. Yang, H. Keshavan, M.W. Barsoum, Bonding and oxidation protection of Ti_2AlC and Cr_2AlC for a Ni-based superalloy, J. Eur. Ceram. Soc. 39 (2019) 878–882.
[5] J. Gonzalez-Julian, T. Go, D.E. Mack, R. Vaßen, Environmental resistance of Cr_2AlC MAX phase under thermal gradient loading using a burner rig, J. Am. Ceram. Soc. 101 (2018) 1841–1846.
[6] S. Hu, S. Li, H. Li, Y. Zhou, Oxyacetylene torch testing and microstructural characterization of a Cr_2AlC ceramic, J. Alloys. Compd. 740 (2018) 77–81.
[7] J.C. Schuster, H. Nowotny, C. Vaccaro, The ternary system: Cr-Al-C, V-Al-C, and Ti-Al-C and the behavior of H-phases (M_2AlC), J. Solid State Chem. 32 (1980) 213–219.
[8] Q. Huang, H. Han, R. Liu, G. Lei, L. Yan, J. Zhou, Q. Huang, Saturation of ion irradiation effects in MAX phase Cr_2AlC, Acta Mater. 110 (2016) 1–7.

[9] C. Tang, M. Stueber, H.J. Seifert, M. Steinbrueck, Protective coatings on zirconium-based alloys as accident-tolerant fuel (ATF) claddings, Corros. Rev. 35 (2017) 141–165.
[10] J.L. Smialek, J.A. Nesbitt, T.P. Gabb, A. Garg, R.A. Miller, Hot corrosion and low cycle fatigue of a Cr_2AlC-coated superalloy, Mater. Sci. Eng.: A 711 (2018) 119–129.
[11] Q.M. Wang, R. Mykhaylonka, A. Flores Renteria, J.L. Zhang, C. Leyens, K.H. Kim, Improving the high-temperature oxidation resistance of a β–γ TiAl alloy by a Cr_2AlC coating, Corros. Sci. 52 (2010) 3793–3802.
[12] J.J. Li, M.S. Li, H.M. Xiang, X.P. Lu, Y.C. Zhou, Short-term oxidation resistance and degradation of Cr_2AlC coating on M38G superalloy at 900-1100 °C, Corros. Sci. 53 (2011) 3813–3820.
[13] Z.J. Lin, M.S. Li, J.Y. Wang, Y.C. Zhou, High-temperature oxidation and hot corrosion of Cr_2AlC, Acta Mater. 55 (2007) 6182–6191.
[14] S. Li, X. Chen, Y. Zhou, G. Song, Influence of grain size on high temperature oxidation behavior of Cr_2AlC ceramics, Ceram. Int. 39 (2013) 2715–2721.
[15] B. Cui, D.D. Jayaseelan, W.E. Lee, Reply to comment on "Microstructural evolution during high-temperature oxidation of Ti_2AlC ceramics", Scripta Mater. 65 (2011) 933–934.
[16] R.M. Langford, A.K. Petford-Long, Preparation of transmission electron microscopy cross-section specimens using focused ion beam milling, J. Vac. Sci. Technol. A 19 (2001) 2186–2193.
[17] T.C. Santini, Application of the Rietveld refinement method for quantification of mineral concentrations in bauxite residues (alumina refining tailings), Int. J. Miner. Process. 139 (2015) 1–10.
[18] J.J. Li, Y.H. Qian, D. Niu, M.M. Zhang, Z.M. Liu, M.S. Li, Phase formation and microstructure evolution of arc ion deposited Cr_2AlC coating after heat treatment, Appl. Surf. Sci. 263 (2012) 457–464.
[19] Z.Y. Wang, J.Z. Liu, L. Wang, X.W. Li, P.L. Ke, A.Y. Wang, Dense and high-stability Ti_2AlN MAX phase coatings prepared by the combined cathodic arc/sputter technique, Appl. Surf. Sci. 396 (2017) 1435–1442.
[20] C. Wang, W. Zhang, Z. Han, L. Shi, Behaviors of helium in Cr_2AlC from first principles, J. Am. Ceram. Soc. 101 (2018) 5771–5780.
[21] A.M. Huntz, Parabolic laws during high temperature oxidation: relations with the grain size and thickness of the oxide, J. Mater. Sci. Lett. 18 (1999) 1981–1984.
[22] M. Haftani, M. Saeedi Heydari, H.R. Baharvandi, N. Ehsani, Studying the oxidation of Ti_2AlC MAX phase in atmosphere: a review, Int. J. Refract. Metals Hard Mater. 61 (2016) 51–60.
[23] X.K. Qian, X.D. He, Y.B. Li, Y. Sun, H. Li, D.L. Xu, Cyclic oxidation of Ti_3AlC_2 at 1000–1300 °C in air, Corros. Sci. 53 (2011) 290–295.
[24] D.J. Tallman, B. Anasori, M.W. Barsoum, A critical review of the oxidation of Ti_2AlC, Ti_3AlC_2 and Cr_2AlC in air, Mater. Res. Lett. 1 (2013) 115–125.
[25] P. Ren, Y. Yang, S. Zhu, F. Wang, Effect of Ti on the microstructure change and oxidation behavior of Ni + CrAlYHfSiN composite coatings, Corros. Sci. 150 (2019) 54–63.
[26] W. Tian, P. Wang, Y. Kan, G. Zhang, Oxidation behavior of Cr_2AlC ceramics at 1100 and 1250 °C, J. Mater. Sci. 43 (2008) 2785–2791.
[27] N. Babu, R. Balasubramaniam, A. Ghosh, High-temperature oxidation of Fe_3Al based iron aluminides in oxygen, Corros. Sci. 43 (2001) 2239–2254.
[28] Q. Luo, S.C. Wang, Z. Zhou, L. Chen, Structure characterization and tribological study of magnetron sputtered nanocomposite nc-TiAlV(N,C)/a-C coatings, J. Mater. Chem. 21 (2011) 9746–9756.
[29] Y.-X. Xu, M. Chirol, C.-J. Li, A. Vardelle, Formation of Al_2O_3 diffusion barrier in cold-sprayed NiCoCrAlY/Ni multi-layered coatings on 304SS substrate, Surf. Coat. Technol. 307 (2016) 603–609.
[30] S.H. Hosseini, S. Mirdamadi, S. Rastegari, Investigating efficiency of α-Al_2O_3 diffusion barrier layer in oxidation of EB-PVD NiCrAlY coatings, Surf. Eng. 31 (2014) 146–155.
[31] R.S.J.S. Park, J.H. Perepezko, Coating designs for oxidation control of Mo–Si–B alloys, Scripta Mater. 46 (2002) 765–770.
[32] J.M. Schneider, Z. Sun, R. Mertens, F. Uestel, R. Ahuja, Ab initio calculations and experimental determination of the structure of Cr_2AlC, Solid State Commun. 130 (2004) 445–449.
[33] Q.M. Wang, A. Flores Renteria, O. Schroeter, R. Mykhaylonka, C. Leyens, W. Garkas, M. to Baben, Fabrication and oxidation behavior of Cr_2AlC coating on Ti6242 alloy, Surf. Coat. Technol. 204 (2010) 2343–2352.
[34] H. Zhen, X. Peng, A new approach to manufacture oxidation-resistant NiCrAl overlay coatings by electrodeposition, Corros. Sci. 150 (2019) 121–126.
[35] H.-Z. Yang, J.-P. Zou, Q. Shi, M.-J. Dai, S.-S. Lin, W. Du, L. Lv, Analysis of the microstructural evolution and interface diffusion behavior of NiCoCrAlYTa coating in high temperature oxidation, Corros. Sci. 153 (2019) 162–169.
[36] S. Ma, J. Ye, A. Liu, Y. Liu, J. Wang, J. Pang, I. Reimanis, Synthesis, Characterization, and Consolidation of $Cr_2(C,N)$ Solid Solution Powders, J. Am. Ceram. Soc. 99 (2016) 1943–1950.
[37] O. Berger, R. Boucher, M. Ruhnow, Part I. Mechanism of oxidation of Cr_2AlC films in temperature range 700-1200°C, Surf. Eng. 31 (2014) 373–385.
[38] O. Berger, R. Boucher, M. Ruhnow, Part II. Oxidation of yttrium doped Cr_2AlC films in temperature range between 700 and 1200 °C, Surf. Eng. 31 (2014) 386–396.
[39] D.B. Lee, S.W. Park, Oxidation of Cr_2AlC Between 900 and 1200 °C in Air, Oxid. Met. 68 (2007) 211–222.